J. Fluid Mech. (2003), *vol.* 494, *pp.* 95–117.
DOI: 10.1017/S0022112003005974 Printed in the United Kingdom

Three-dimensional miscible displacement simulations in homogeneous porous media with gravity override

By A. RIAZ AND E. MEIBURG†

Department of Mechanical and Environmental Engineering, University of California, Santa Barbara, CA 93106, USA

(Received 4 November 2002 and in revised form 27 May 2003)

High-accuracy three-dimensional numerical simulations of miscible displacements with gravity override in homogeneous porous media are carried out for the quarter five-spot configuration. Special emphasis is placed on describing the influence of viscous and gravitational effects on the overall displacement dynamics in terms of the vorticity variable. Even for neutrally buoyant displacements, three-dimensional effects are seen to change the character of the flow significantly, in contrast to earlier findings for rectilinear displacements. At least in part this can be attributed to the time dependence of the most dangerous vertical instability mode. Density differences influence the flow primarily by establishing a narrow gravity layer, in which the effective Péclet number is enhanced owing to the higher flow rate. However, buoyancy forces of a certain magnitude can lead to a pinch-off of the gravity layer, thereby slowing it down. Overall, an increase of the gravitational parameter is found to enhance mostly the vertical perturbations, while larger *Pe* values act towards amplifying horizontal disturbances. The asymptotic rate of growth of the mixing length varies only with Péclet number. For large Péclet numbers, an asymptotic value of 0.7 is observed. A scaling law for the thickness of the gravity layer is obtained as well. In contrast to immiscible flow displacements, it is found to increase with the gravity parameter.

1. Introduction

The stability of interfaces separating fluids of different viscosities in porous media has been the subject of numerous investigations over the years, ever since the pioneering work of Hill (1952), Saffman & Taylor (1958) and Chouke, Meurs & Poel (1959) established that an adverse mobility ratio, i.e. a less viscous fluid displacing a more viscous one, generates an unstable interface. By means of experiments and, more recently, numerical simulations, the nonlinear interfacial dynamics has been studied as well, using a variety of physical models and geometries, cf. the review by Homsy (1987). In many physical applications, the basic instability due to the viscosity contrast is influenced by density and permeability variations as well. The overall displacement process is then governed by a combination of these three contributions.

For *unidirectional* base flows, a number of numerical investigations have addressed the above issues in both two and three dimensions, among them Christie & Bond

† Author to whom correspondence should be addressed.

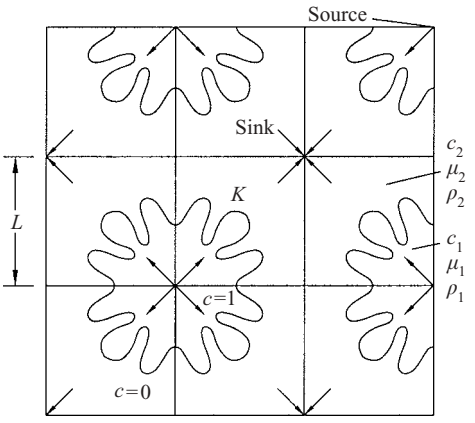

FIGURE 1. The quarter five-spot arrangement of injection and production wells.

(1987), Tan & Homsy (1988), Zimmerman & Homsy (1992*a*), Tchelepi & Orr, (1993, 1994), and Ruith & Meiburg (2000). On the other hand, problems involving line source injection, which occurs frequently during secondary oil recovery processes, have not received comparable attention. In doubly periodic arrangements of injection and production wells such as the well-known quarter five-spot configuration shown in figure 1, *spatially varying* base flows exist that give rise to effects absent in unidirectional flows, cf. the two-dimensional investigations by Chen & Meiburg (1998*a*, *b*) Hence the present investigation focuses on variable viscosity and density, miscible displacements in homogeneous permeability, three-dimensional quarter five-spot domains.

Early experiments in the quarter five-spot configuration, carried out by Simmons *et al.* (1959), Caudle & Witte (1959), Lacey, Faris & Brinkman (1961) and Habermann (1960), demonstrated the decrease in displacement efficiency for adverse mobility ratios. While these authors observe fingering patterns that are qualitatively similar to those documented in the rectilinear experiments by Slobod & Thomas (1963), Perkins, Johnston & Hoffman (1965) and Wooding (1969), there are important differences in the way the governing mechanisms interact in these different geometries. As pointed out by Chen & Meiburg (2000), highly accurate numerical simulations for displacements with line sources and sinks are significantly more difficult than for their rectilinear counterparts, owing to the presence of the singularities, large variations in the velocities, and potential grid orientation effects, cf. Brand, Heinemann & Aziz (1991). Some of the early investigations, e.g. Sherwood (1987), Fayers, Blunt & Christie (1992) and Bradvedt *et al.* (1992) did not account for physical diffusion or velocity induced dispersion, and instead let the computational grid provide a small-scale cutoff by means of numerical diffusion. Tan & Homsy (1988), on the other hand, showed that a high-accuracy Fourier spectral method can reproduce all physically relevant length scales in simulations of rectilinear flows. Chen & Meiburg (1998*a*, *b*, 2000) demonstrated that a combination of spectral methods and high-order compact finite differences can be employed to obtain very high accuracy in simulations of two-dimensional quarter five-spot simulations as well. The present investigation extends this approach to three dimensions, in order to analyse the interaction of viscous and gravitational effects in such configurations. While some preliminary phenomenological observations were presented by Riaz & Meiburg (2002), the goal of the present more comprehensive analysis is to study in detail the fundamental

physical mechanisms related to various parameter regimes in terms of the interactions between the horizontal and the vertical modes, as well as the interaction of viscous and gravitational vorticity fields.

The paper is organized as follows. Section 2 presents the governing equations, as well as boundary and initial conditions. Section 3 discusses the numerical implementation, as well as validation results. Section 4 compares neutrally buoyant, two- and three-dimensional displacements. The existence of significant differences between the two is pointed out, which is in contrast to rectilinear flows. Section 5 presents the results of a parametric study, in which the effects of variations in the governing dimensionless quantities are investigated from a vorticity-based point of view. Section 6 takes a closer look at such integral measures as the temporal evolution of the mixing length and the total interfacial area. Finally, § 7 highlights the main findings of this investigation and summarizes its most important conclusions.

2. Governing equations

The quarter five-spot arrangement consists of a staggered doubly periodic array of injection and production wells, as shown in figure 1. We simulate the miscible, incompressible flow through a homogeneous porous medium in such a configuration on the basis of Darcy's law. The evolution of the scalar concentration field is governed by a convection–diffusion equation, so that we can write the set of governing equations as

$$\nabla \cdot \boldsymbol{u} = 0, \tag{2.1}$$

$$\nabla p = -\frac{\mu}{K}\boldsymbol{u} - \rho \boldsymbol{g}, \tag{2.2}$$

$$\frac{\partial c}{\partial t} + \boldsymbol{u} \cdot \nabla c = D\nabla^2 c. \tag{2.3}$$

Here, $\boldsymbol{u}$ represents the velocity vector, p the pressure, and c the concentration of the injected fluid. The terms μ and ρ denote the dynamic viscosity and density of the fluid, respectively, while K is the constant permeability of the homogeneous porous medium. $\boldsymbol{g}$ indicates the vector of acceleration due to gravity, and D is the molecular diffusion coefficient. Note that in the present work the effects of flow-induced dispersion at the pore scale (Taylor 1953; Horne & Rodriguez 1983; Brady & Koch 1988) are not accounted for. Although velocity related dispersion is known to be important in porous media, an accurate physics-based model for variable density and viscosity displacements is presently not available. Yortsos & Zeybek (1988) and Zimmerman & Homsy (1992*b*) have attempted to account for dispersion in terms of a Taylor dispersion model. However, Petitjeans *et al.* (1999) demonstrate the limited validity of this approach. As a result, the present work accounts for molecular diffusion only, rather than employing a dispersion model that is known to have serious shortcomings. This approach also offers the advantage that we will be able to make comparisons with corresponding earlier two-dimensional simulations of several other authors.

2.1. *Scaling*

The symmetry properties of the quarter five-spot arrangement allow us to limit the computational domain to one periodic element of lateral extent L and height H, respectively, cf. figure 2. Here the indices '1' and '2' refer to the injected and displaced fluid, respectively. In order to render the above set of equations dimensionless, we choose L as the characteristic length scale. By denoting the source strength per unit

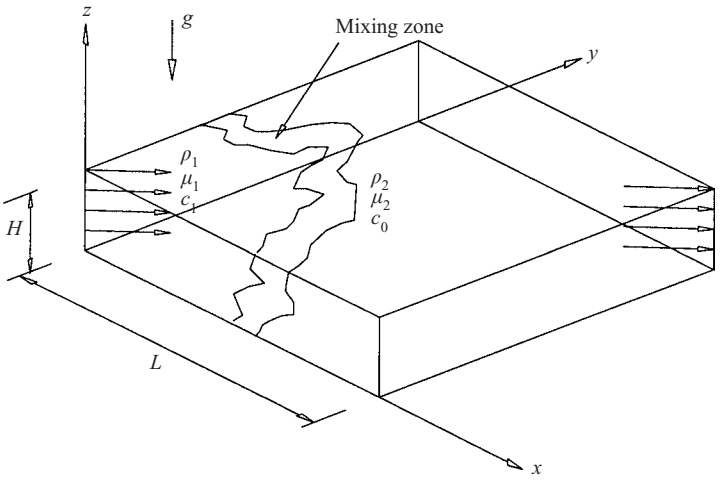

FIGURE 2. The three-dimensional computational domain.

depth as $2\pi Q$, we thus obtain time and velocity scales as L^2/Q and Q/L, respectively. The characteristic pressure scales as $\mu_1 Q/K$. The viscosity μ_1 of the injected fluid is taken as the characteristic value for scaling the viscosities, while the difference in the fluid densities $\rho_2 - \rho_1$ provides a characteristic density value. We thus can define an aspect ratio $A = H/L$, and obtain the dimensionless set of governing equations of the form

$$\nabla \cdot \boldsymbol{u} = 0, \tag{2.4}$$

$$\nabla p = -\mu \boldsymbol{u} - G\rho \nabla z, \tag{2.5}$$

$$\frac{\partial c}{\partial t} + \boldsymbol{u} \cdot \nabla c = \frac{1}{Pe} \nabla^2 c. \tag{2.6}$$

Here, the Péclet number,

$$Pe = \frac{Q}{D}, \tag{2.7}$$

indicates the relative importance of convective and diffusive effects for the evolution of the concentration field. The gravity parameter,

$$G = \frac{g(\rho_2 - \rho_1) K L}{Q \mu_1}, \tag{2.8}$$

represents a measure of the strength of buoyancy forces relative to viscous forces. The dimensionless fluid density is assumed to vary linearly with concentration according to

$$\rho = \frac{\rho_2}{\rho_2 - \rho_1} - c.$$

By using this relation in (2.5) and absorbing the constant term in the pressure, we obtain

$$\nabla p = -\mu \boldsymbol{u} + Gc \nabla z. \tag{2.9}$$

Following earlier authors, we assume an exponential dependence of the fluid viscosity on the concentration according to

$$\mu = \mathrm{e}^{R(1-c)}, \tag{2.10}$$

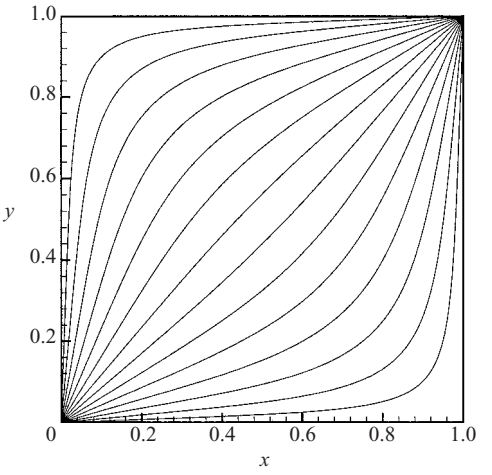

FIGURE 3. Streamlines of the potential velocity field $\boldsymbol{u}_{pot}$.

where the mobility ratio

$$R = -\frac{1}{\mu}\frac{\mathrm{d}\mu}{\mathrm{d}c} = \ln\left(\frac{\mu_2}{\mu_1}\right). \tag{2.11}$$

2.2. *Vorticity-vector potential formulation*

For the purpose of numerically solving the governing equations, we recast Darcy's law into the vorticity variable by taking the curl of (2.5)

$$\omega = R\nabla c \times \boldsymbol{u} + \frac{G}{\mu}\nabla c \times \nabla z. \tag{2.12}$$

This approach has been taken by other authors before (Tryggvason & Aref 1985; Meiburg & Homsy 1988*a*, *b*; Tan & Homsy 1988; Zimmerman & Homsy 1992*b*; Rogerson & Meiburg 1993*a*; De Wit & Homsy 1997*b*; Chen & Meiburg 1998*a*; Pankiewitz & Meiburg 1999; Ruith & Meiburg 2000). It allows us to distinguish between viscosity and density variations as potential sources of vorticity, and thereby of velocity. This will represent a valuable tool in the physical interpretation of the computational results. Following our earlier investigation of two-dimensional miscible displacements in the quarter five-spot geometry (Chen & Meiburg 1998*a*, *b*; Pankiewitz & Meiburg 1999), we decompose the velocity field into a steady, potential component $\boldsymbol{u}_{pot}(x, y)$, cf. figure 3, and an unsteady, rotational one $\boldsymbol{u}_{rot}(x, y, z, t)$. The potential flow field shown in figure 3 represents a spatially varying base state which is obtained analytically from a doubly periodic array of point sources and sinks (Morel-Seytoux 1965). In order to avoid numerical instabilities due to excessively large velocities near the injection and production wells, we replace the singular distribution of the source and sink strength in the computational domain by a Gaussian distribution of radius 0.05. The rotational velocity component is smooth everywhere and can be obtained with a high degree of accuracy, as will be described below.

The rotational velocity field is related to a three-dimensional vector potential as

$$\boldsymbol{u}_{rot} = \nabla \times \psi \ . \tag{2.13}$$

This vector potential in turn can be determined from the vorticity as

$$\nabla^2 \psi = -\omega \tag{2.14}$$

or, in component form,

$$\nabla^2 \begin{pmatrix} \phi \\ \theta \\ \chi \end{pmatrix} = - \begin{pmatrix} \xi \\ \eta \\ \zeta \end{pmatrix}. \tag{2.15}$$

2.3. *Boundary and initial conditions*

The following relations reflect the symmetry and no-flux boundary conditions at the borders of the computational domain

$$x = 0, 1 : \begin{cases} c_x = 0, & & \\ u = 0, & v_x = 0, & w_x = 0, \\ \phi_x = 0, & \theta = 0, & \chi = 0, \\ \xi_x = 0, & \eta = 0, & \zeta = 0, \end{cases} \tag{2.16}$$

$$y = 0, 1 : \begin{cases} c_y = 0, & & \\ u_y = 0, & v = 0, & w_y = 0, \\ \phi = 0, & \theta_y = 0, & \chi = 0, \\ \xi = 0, & \eta_y = 0, & \zeta = 0, \end{cases} \tag{2.17}$$

$$z = 0, A : \begin{cases} c_z = 0 & w = 0, & \\ \phi = 0, & \theta = 0, & \chi_z = 0. \end{cases} \tag{2.18}$$

In order to avoid starting with a singular concentration distribution at time $t = 0$, we specify as the initial condition a concentration profile that can be obtained as a self-similar solution to the radially symmetric problem (Tan & Homsy 1987). It has the form

$$c_0 = \frac{1}{2}\left[1 + \mathrm{erf}\left(\sqrt{Pe}\left(\frac{r}{r_0} - 1\right)\right)\right]. \tag{2.19}$$

Here r_0 represents the initial radial location of the front. It determines the 'effective starting time' $t_0 > 0$ of the computation

$$t_0 = 0.5\, r_0^2. \tag{2.20}$$

We use $t_0 = 0.02$ throughout. This starting time is selected to compare with the earlier two-dimensional work of Chen & Meiburg (1998*a*), who also conduct a sensitivity analysis of the starting time.

3. Numerical implementation and validation

The numerical solutions are obtained with a combination of sixth-order compact finite difference (Lele 1992) and spectral methods (Gottlieb & Orszag 1977; Canuto *et al.* 1986), in conjunction with an explicit third-order time-stepping scheme.

3.1. *Time-stepping scheme*

The concentration field is advanced in time by an explicit third-order Runga–Kutta method (Wray 1991). Writing the concentration equation (2.6) as

$$\frac{\partial c}{\partial t} = F(c)\ , \tag{3.1}$$

we obtain

$$c_{i,j}^{k} = c_{i,j}^{k-1} + \Delta t\left[\alpha_k F\left(c_{i,j}^{k-1}\right) + \beta_k F\left(c_{i,j}^{k-2}\right)\right], \tag{3.2}$$

where

$$\alpha_1 = \tfrac{8}{15},\ \beta_1 = 0,$$
$$\alpha_2 = \tfrac{5}{12},\ \beta_2 = -\tfrac{17}{60},$$
$$\alpha_3 = \tfrac{3}{4},\ \beta_3 = -\tfrac{5}{12}.$$

3.2. *Solution of the Poisson equation*

The solution procedure for the Poisson equation governing the vector potential is described for the example of the first component

$$\phi_{xx} + \phi_{yy} + \phi_{zz} = -\xi. \tag{3.3}$$

Because of the periodicity in the x- and y-directions, this equation can be solved by a Fourier–Galerkin method. The Fourier coefficients a_{ij} and b_{ij} of the vector potential and vorticity fields, respectively, are given by

$$\phi = \sum_{j=1}^{n}\sum_{i=1}^{n} a_{ij}(z)\cos[(i-1)\pi x]\sin[(j-1)\pi y)], \tag{3.4}$$

$$\xi = \sum_{j=1}^{n}\sum_{i=1}^{n} b_{ij}(z)\cos[(i-1)\pi x]\sin[(j-1)\pi y)]. \tag{3.5}$$

A second-order ODE for $a_{ij}(z)$ is obtained by substituting (3.4) and (3.5) into (3.3)

$$[-(i-1)^2\pi^2 - (j-1)^2\pi^2]a_{ij}(z) + a_{ij}''(z) = -b_{ij}(z). \tag{3.6}$$

By using compact finite differences to approximate $\mathrm{d}^2a/\mathrm{d}z^2$, we obtain the following pentadiagonal system

$$\alpha(a_{i,j,k-2} + a_{i,j,k+2}) + \beta(a_{i,j,k-1} + a_{i,j,k+1}) + \gamma a_{i,j,k} = -\tfrac{2}{11}b_{i,j,k-1} - b_{i,j,k} - \tfrac{2}{11}b_{i,j,k+1},$$

where

$$\alpha = \frac{3}{44\Delta^2},$$
$$\beta = -\tfrac{2}{11}[(i-1)^2 + (j-1)^2]\pi^2 + \frac{12}{11\Delta^2},$$
$$\gamma = -[(i-1)^2 + (j-1)^2]\pi^2 - \tfrac{24}{11}\Delta^2 - \frac{3}{22\Delta^2}.$$

A fine spatial and temporal resolution is required in order to resolve accurately all the length scales present in the domain, especially at high Péclet numbers. Time steps as small as $O(10^{-6})$ are used, while typical spatial resolutions employ $256 \times 256 \times 32$ modes, i.e. 2×10^6 grid points. For some parameter values, a spatial resolution of $513 \times 513 \times 64$ will be used. A preliminary analysis was conducted to determine the appropriate grid spacing for different parameter combinations. An important criterion in this regard is the cutoff mode provided by the linear stability analysis (Tan & Homsy 1987; Riaz & Meiburg 2003). The grid spacing is required always to be smaller than the cutoff wavelength. In addition, we also track the energy in the highest Fourier mode and require it to be less than 0.001% of the maximum energy in the

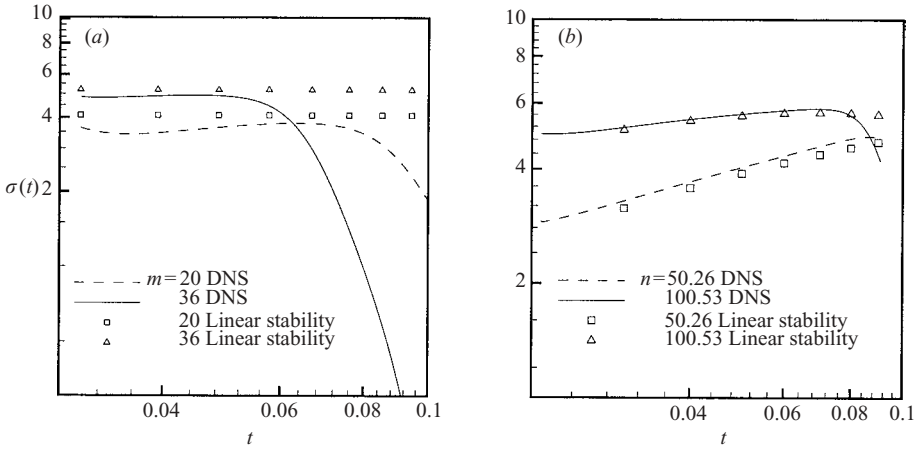

FIGURE 4. Comparison of the growth rates obtained from the simulation data with corresponding linear stability results for different wavenumbers of (*a*) azimuthal and (*b*) vertical perturbations, and $Pe = 400$, $R = 2.5$, $G = 0$.

spectrum. We also require the maximum and minimum numerical concentration levels to remain between 1.001 and −0.001, respectively. We have found these particular values of the constraints to guarantee convergence and stability of the numerical results. Our numerical algorithm is parallelized for optimal performance (Riaz 2003).

3.3. *Validation*

In order to demonstrate the validity and accuracy of our results, we compare computational data for the growth rates of azimuthal and vertical perturbation waves in neutrally buoyant flows with corresponding linear stability results obtained by Tan & Homsy (1987) and Riaz & Meiburg (2003) for radial source flows. Those investigations showed the wavenumbers and growth rates to be determined by both the viscosity ratio and the Péclet number. Even though the base velocity in the quarter five-spot geometry is not strictly radial, it is approximately so during the early stages, when the front is close to the source. Consequently, excellent agreement was obtained between the simulations of Chen & Meiburg (1998*a*) for the growth of azimuthal waves in two-dimensional quarter five-spot flows and the corresponding linear stability results of Tan & Homsy (1987).

For validation purposes we conducted simulations in which the initial concentration fields contained purely vertical or azimuthal, small amplitude (0.001) perturbation waves. Their growth rates are then compared with the respective linear stability analyses. The validation runs were carried out with an aspect ratio $A = 1/8$, a grid size of $257 \times 257 \times 32$, and a time step of $O(10^{-6})$. The concentration front initially is positioned at a radius $r_0 = 0.2$, i.e. a starting time of $t_0 = 0.02$. Figure 4(*a*) presents results for initial azimuthal perturbations of wavenumbers 20 and 36. In the numerical simulations, the growth rate of the disturbances is obtained from the instantaneous slope of the vertical vorticity norm, which is defined as

$$\|\omega(t)\| = \sqrt{\frac{1}{L\,N\,M}\sum_{i=1}^{L}\sum_{j=1}^{N}\sum_{k=i}^{M}\omega(t)_{i,j,k}^2}. \tag{3.7}$$

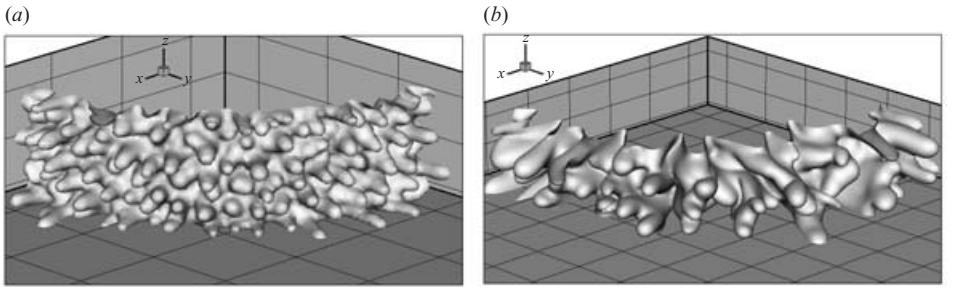

FIGURE 5. Concentration iso-surfaces obtained for random initial perturbations and $G = 0$, $Pe = 800$, $R = 2.5$ and $A = 1/8$, at times (a) 0.04 and (b) 0.14. Nonlinear interaction mechanisms of merging, shielding and fading can be observed.

Here, L, M and N denote the number of grid points in the x-, y- and z-directions, respectively. Figure 4(a) indicates good agreement between the simulation and stability analysis data for early times. For long times, nonlinear effects become relevant, so that the simulation data increasingly deviate from the linear stability growth rates.

The corresponding comparison for axial waves is shown in figure 4(b). Again, reasonable agreement is observed for the time-dependent growth rates between the simulation data and the linear stability results of Riaz & Meiburg (2003). In this context, it is important to mention that an exact agreement with numerics and linear theory is not to be expected, since the latter is based on the quasi-steady state assumption (QSSA). The recent work by Ben, Demekhin & Chang (2002) provides a first-order correction to the QSSA growth rates for rectilinear flows, which shows that the QSSA becomes increasingly valid for later times, as expected. A similar correction to the QSSA for radial flows is not available at present.

4. Comparison between two- and three-dimensional neutrally buoyant displacements

For a neutrally buoyant displacement without externally imposed initial perturbations in the vertical direction, the present three-dimensional algorithm exactly reproduces the two-dimensional results reported by Chen & Meiburg (1998a). In order to trigger a three-dimensionally evolving flow, we introduce random initial concentration perturbations of the form

$$c(x, y, z, t_0) = c_0(x, y, t_0) + \gamma f(x, y, z) \exp(-(r - r_0)^2/\sigma^2). \tag{4.1}$$

Here, γ denotes the disturbance amplitude, f represents a field of random numbers uniformly distributed in the interval $[-1, 1]$, and σ specifies the width of the initially perturbed layer around the mean interface position r_0. The simulations to be discussed below employ $\gamma = 0.025$ and $\sigma = 0.003$, as well as an initial interface location of $r_0 = 0.2$.

Random initial perturbations of the above form give rise to substantial fingering activity from the very start. Figure 5 presents a simulation for $Pe = 800$, $R = 2.5$ and $G = 0$, i.e. without density contrast. The number of fingers in both the horizontal and vertical planes at early times are consistent with the linear stability results, as shown in figure 5(a). The number of fingers is greatly reduced at later times, as seen in figure 5(b). This is expected both on the basis of linear stability results for vertical

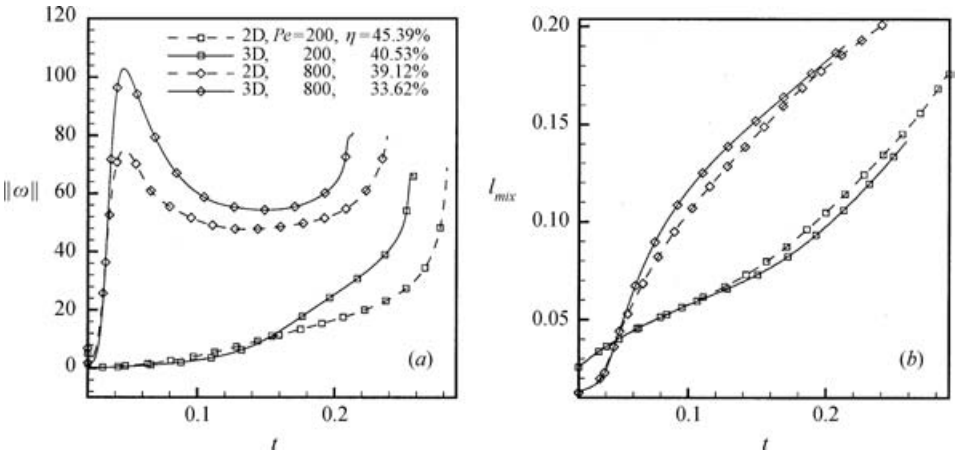

FIGURE 6. (*a*) Comparison of the vorticity norm for the two- and three-dimensional cases for two different Péclet numbers. Higher vorticity values in the three-dimensional case result in a lower efficiency as compared to the two-dimensional case for both small and large *Pe*. The higher vorticity level in the three-dimensional case results from the additional instability towards axial waves (Riaz & Meiburg 2003). (*b*) Mixing length for the two- and three-dimensional cases. This global measure of the displacement dynamics is relatively less sensitive to three-dimensional effects.

modes, and owing to the nonlinear mechanisms of finger interaction, i.e. merging and shielding (Tan & Homsy 1988).

A quantitative comparison between the two- and three-dimensional displacements is given in figure 6. The higher vorticity level in the three-dimensional simulation reflects a strong finger growth, which eventually leads to an earlier breakthrough as shown in figure 6. Here, the breakthrough time t_b is defined as the time when the concentration of the injected fluid first reaches 1% somewhere along the height of the production well. Correspondingly, the overall efficiency η of the displacement process is given as the fraction of the total domain volume occupied by the injected fluid at the time of breakthrough, $\eta = \pi t_b/2$.

Another important global diagnostic of miscible displacement processes is the mixing length, cf. the more detailed discussion in § 6.1. Figure 6(*b*) shows that the mixing lengths for the two cases are quite similar, although a slightly higher value for the three-dimensional case can be observed for $Pe = 800$. Thus, this global measure of the displacement dynamics is seen to be less sensitive to three-dimensional effects. However, the comparison of the vorticity magnitude in figure 6(*a*) indicates a significant difference between two- and three-dimensional displacements in the quarter five-spot geometry, even for neutrally buoyant flows. This is somewhat unexpected in light of the findings by Zimmerman & Homsy (1992*a*) and Tchelepi (1994), who had observed only small differences between two- and three-dimensional rectilinear flows. Zimmerman & Homsy (1992*a*) attributed this to the lack of a vortex stretching term in Darcy's flow, since it is this term that causes quite fundamental differences between two- and three-dimensional flows governed by the Navier–Stokes equations. For quarter-spot displacements on the other hand, the higher vorticity level for three-dimensional displacements is due to an effective redistribution of the concentration gradient associated with the changes in the wavelength ratio of the most amplified vertical and horizontal waves (Riaz & Meiburg 2003). Consequently, higher overall

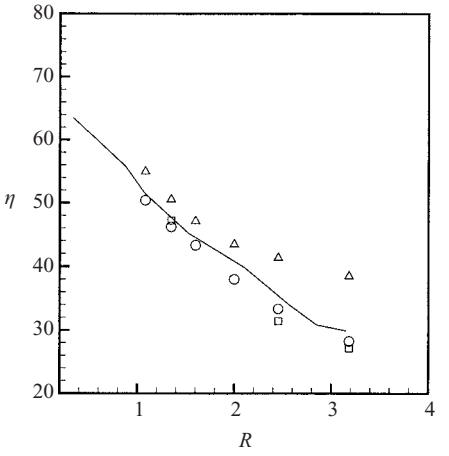

FIGURE 7. Displacement efficiency as a function of the viscosity ratio. —, experimental data by Habermann (1960) and □, Zhang, Sorbie & Tsibuklis (1997) are compared with △, numerical two-dimensional data for $Pe = 800$ (obtained with the present three-dimensional code using two-dimensional initial perturbations), and with ○, the present three-dimensional data for $Pe = 800$. The three-dimensional results exhibit significantly better agreement with the experimental data.

concentration fluctuations than in the purely two-dimensional case generate faster growing fingers for the three-dimensional case, which lead to an earlier breakthrough.

The influence of different realizations of the random initial concentration perturbations as far as neutrally buoyant disturbances are concerned is not significant. We carried out 20 different runs for the parameter combination of the flow shown in figure 5. The breakthrough times varied by less than $\pm 3\%$. In addition, varying γ and σ changed the breakthrough times by less than $\pm 1\%$. The particular values of γ and σ employed here represent the minimum necessary for generating substantial three-dimensional structures for the present combination of governing dimensionless parameters.

In order to demonstrate the validity of the simulations for the nonlinear stages, figure 7 compares the present two- and three-dimensional simulation data for the displacement efficiency with the experimental results of Zhang *et al.* (1997) and Habermann (1960). The experiments quoted do not provide sufficient information to calculate a Péclet number. However, numerical simulations performed at $Pe = 800$ agree reasonably well with the experimental data for different viscosity ratios. The three-dimensional simulations are seen to lead to better agreement than their two-dimensional counterparts, especially at high viscosity ratios. Different Pe values result in somewhat different values of η; however, the trend of a continued decrease in η with R at large R values is more accurately represented by the three-dimensional simulations, independent of Pe. Similarly, the inclusion of a dispersion model would be expected to result in somewhat different values of η.

Three-dimensional simulations more accurately represent the displacement process by accounting for the interaction between the horizontal and the vertical modes. We quantify this interaction by analysing the relative magnitude of the norm for the vertical and the horizontal components of viscous vorticity. Figure 8 shows that the horizontal modes, associated with vertical vorticity, dominate at an early time of $t < 0.05$ for both $Pe = 200$ and 400, when $\|\omega^{\mathrm{v}}\|/\|\omega^{\mathrm{h}}\| > 1$. However, the negative slope

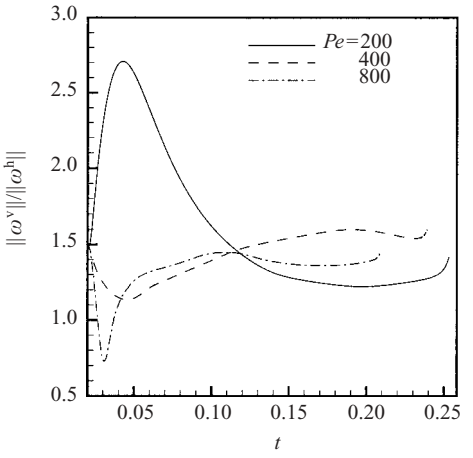

FIGURE 8. Ratio of the vertical to the horizontal vorticity norm for various values of Pe, $R = 2.5$, $G = 0$, $A = 1/8$. $\|\omega^v\|/\|\omega^h\|$ gives the relative strength of the horizontal and the vertical disturbances, respectively. For initial time $t < 0.05$, horizontal modes dominate for $Pe = 200$ while vertical modes gain in strength for $Pe = 400$ and 800. A minimum value of the ratio is observed for $t > 0.12$ as a function of Pe.

of $\|\omega^v\|/\|\omega^h\|$ for $Pe = 400$ and early times shows that the energy in the vertical modes is growing at a higher rate. For $Pe = 800$, the ratio soon drops below 1, indicating the dominance of the vertical modes. This relative importance of the vertical modes at early times for $Pe = 400$ and 800 is predicted by linear stability theory, cf. Riaz & Meiburg (2003). The situation subsequently changes owing to the onset of nonlinear behaviour. It is important to note that for later times $\|\omega^v\|/\|\omega^h\| > 1$, which indicates that the horizontal modes play a relatively more important part in the displacement dynamics. Also, note that at later times, $\|\omega^v\|/\|\omega^h\|$ exhibits a minimum. This reflects the fact that for large Pe values the strength of the vertical vorticity is reduced as a result of nonlinear interactions among the horizontal modes. The dominance of the horizontal modes is due to the mean flow in the horizontal planes. Further simulations show that $\|\omega^v\|/\|\omega^h\|$ is independent of the aspect ratio, but only for neutrally buoyant displacements. The interaction of the horizontal and vertical modes qualitatively changes in displacements with gravity override, as will be discussed below.

5. Parametric study and vorticity considerations

In the following, we will discuss the influence of the governing dimensionless parameters Pe, G and R on the overall features of the displacement process in a homogeneously permeable domain. How those flows are altered by the effects of density stratification in comparison with the purely viscous instability studied by Chen & Meiburg (1998*a*) will be one of the main issues to be analysed here.

5.1. *Influence of the gravity parameter*

Figure 9 presents concentration contours for the case of $Pe = 800$, $R = 2.5$, $G = 0.5$ and $A = 1/8$, i.e. all parameters except G have the same value as in figure 5. The simulation employs a grid of size $257 \times 257 \times 32$, as well as a time step of $O(10^{-6})$. The injected fluid, being lighter than the displaced fluid, tends to rise towards the

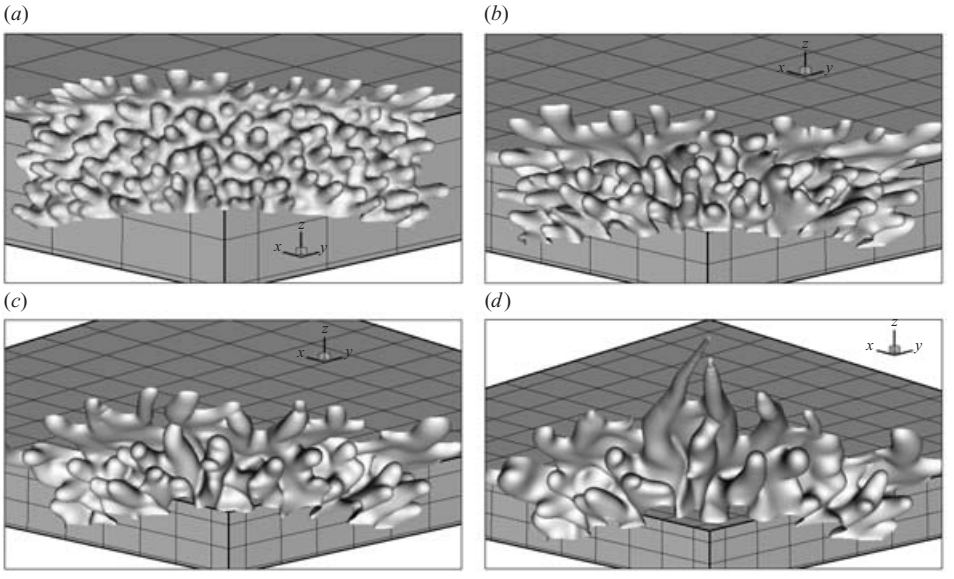

FIGURE 9. Concentration iso-surfaces for $Pe = 800$, $R = 2.5$, $G = 0.5$ and $A = 1/8$ at times (*a*) 0.04, (*b*) 0.08, (*c*) 0.14 and (*d*) 0.21. A gravity layer with numerous fingers evolves early on and becomes dominant around $t = 0.14$. The coupling of viscous and gravitational instability renders the gravity layer susceptible to a pinch-off by the underride fingers. Breakthrough is achieved by fingers in the gravity layer at $t = 0.21$.

upper boundary of the domain. A *gravity layer* is thus established in which the flow rate is higher than elsewhere in the domain. Both the gravity layer and the *underride* region below it give rise to well-developed fingers as early as $t = 0.04$. The number of fingers decreases as the interface evolves owing to both horizontal and vertical interactions among the fingers, cf. figure 9(*b*). The thickness of the gravity layer is seen to increase, owing to multiple mergers with the fingers directly below it. It is important to note the wide range of length scales produced during the displacement.

At $t = 0.14$, the growth of the fingers along the diagonal in the gravity layer is temporarily slowed by fingers approaching from below, cf. figure 9(*c*). The resulting buoyancy-induced pinch-off effect, cf. also Ruith & Meiburg (2000), cuts off the fluid supply of high-velocity fingers in the gravity layer and leads to their gradual fading. This gives a chance to fingers farther away from the diagonal to break through first at $t = 0.21$. The pinch-off mechanism thus delays the time of breakthrough.

Closely related to the structure of the interface is the vorticity field. Equation (2.12) shows that vorticity is generated owing to concentration gradients, which in turn determine the velocity field. Equation (2.12) also shows that gravitational vorticity components can reinforce or cancel directly only the horizontal viscous vorticity components. Figure 10 plots isosurfaces of the viscous and gravitational vorticity components for the flow shown in figure 9. Dark (light) shading represents negative (positive) values of vorticity. The horizontal and vertical components of the viscous vorticity are seen to form elongated dipole structures along the edges of the fingers, while the gravitational vorticity develops a more complex spatial structure. The buoyancy driven pinch-off shown in figures 9(*b*) and 9(*c*) occurs owing to the local reinforcement of the horizontal components of viscous and gravitational vorticity. Note that the spatial distribution of the gravitational vorticity shown in the figure

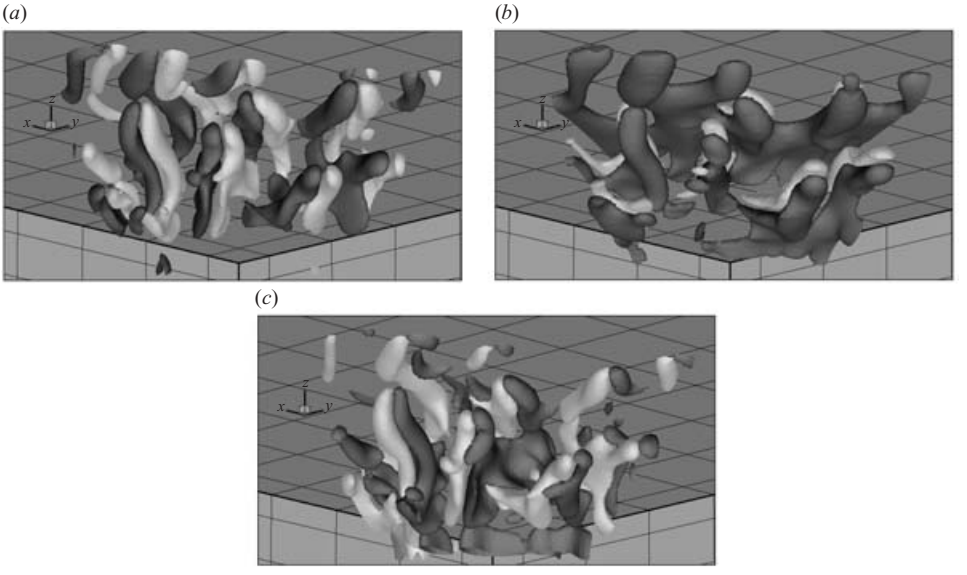

FIGURE 10. Iso-surfaces of (*a*) the vertical viscous, (*b*) horizontal viscous and (*c*) gravitational vorticity components for $Pe = 800$, $R = 2.5$, $G = 0.5$ and $A = 1/8$ at $t = 0.14$. The buoyancy driven interaction occurs because of the local reinforcement of the horizontal components of viscous and gravitational vorticity. The spatial distribution of gravitational vorticity is similar in shape, but of opposite sign to that of the vertical viscous vorticity.

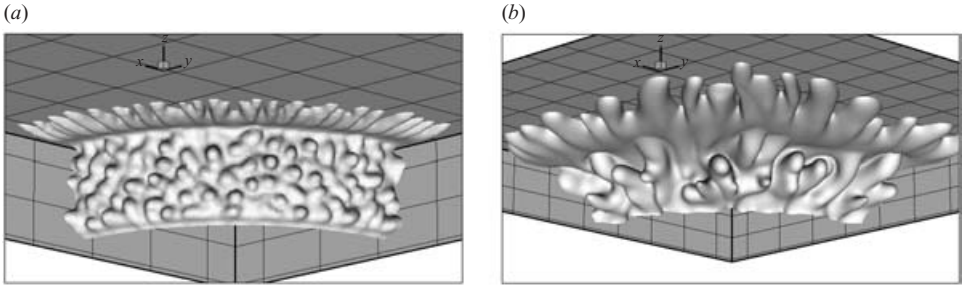

FIGURE 11. Concentration iso-surfaces for $G = 2.0$, $Pe = 800$, $R = 2.5$ and $A = 1/8$ at times (*a*) $t = 0.04$ and (*b*) $t = 0.14$. The gravity layer dominates the displacement. A significant reduction of the fingering activity in the underride region can be observed at this value of G. The breakthrough time is 0.165.

is similar, but of opposite sign to that of the vertical viscous vorticity. This reflects the fact that both the vertical viscous vorticity and the gravitational vorticity are associated with horizontal concentration gradients.

We now consider a situation with a larger density contrast. Figure 11 depicts concentration isosurfaces from a simulation with the same parameter values as above, except that $G = 2$. The mesh size now is $513 \times 513 \times 64$. A strong gravity layer develops in which the effective local Péclet number is large enough to sustain multiple tip splitting events. Most importantly, the gravity layer becomes increasingly dominant and moves far ahead of the underride region. The fingering activity in the underride region is subdued, cf. figures 9(*c*) and 11(*b*). Hence we note that increasing G values stabilize the

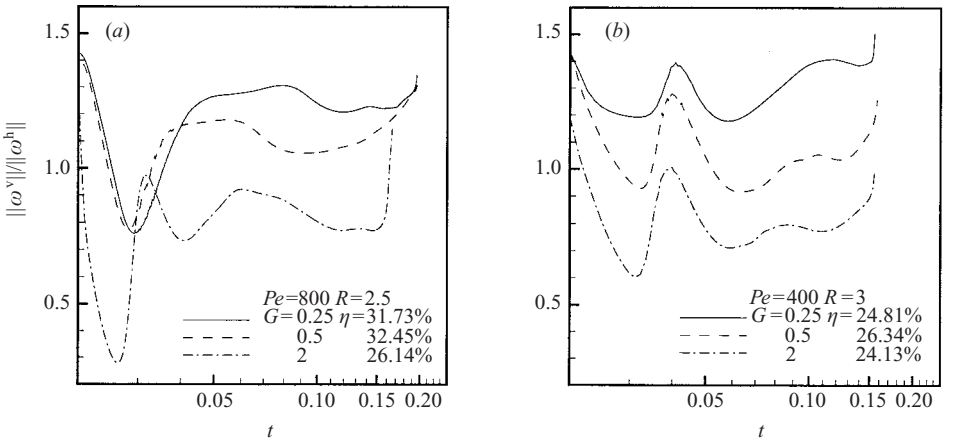

FIGURE 12. Ratio of the norms of vertical to horizontal viscous vorticity components as a function of G. Increase in G uniformly strengthens the vertical component of viscous vorticity. Optimal interaction between the horizontal and the vertical modes is given by $\|\omega^v\|/\|\omega^h\| \approx 1$.

underride region. This form of shear stabilization is studied in detail by Rogerson & Meiburg (1993*b*). In the present case, it has a detrimental effect on the overall efficiency of the displacement process, as it prevents the slowing of the gravity layer by pinch-off events. Consequently, the breakthrough time is reduced by almost 20% as G is increased from 0.5 to 2.

The influence of the gravity override mechanism can be evaluated by considering the relative strengths of waves in the horizontal and vertical directions, as reflected by the ratio of the vertical to the horizontal viscous vorticity in figure 12. It is to be kept in mind that waves in a horizontal plane are associated with vertical vorticity and vice versa. Figure 12(*a*) shows the cases depicted in figures 9 and 11, as well as a case for $G = 0.25$. The ratio $\|\omega^v\|/\|\omega^h\|$ decreases uniformly with an increase in G, reflecting the emergence of a strong gravity layer. Throughout the displacement process, the interplay of vertical and horizontal vorticity components is strongly affected by G. A comparison of the efficiencies listed in figure 12(*a*) shows that the maximum efficiency is achieved at $G = 0.5$, as an optimal interaction between the two components is achieved with the ratio $\|\omega^v\|/\|\omega^h\|$ close to unity throughout the displacement process. A similar optimal behaviour is observed in figure 12(*b*) for $G = 0.5$. A possible interpretation of the optimal interaction phenomena is that the initial dominance of vertical viscous vorticity develops the underride fingers, and the later dominance of buoyancy effects allows these fingers to pinch off the gravity layer. If G is too large, the underride fingers do not develop to a point where a meaningful interaction with the gravity layer can be sustained. On the other hand, if G is too small, the gravity effect is not strong enough to allow the underride fingers to curve upward and pinch off the gravity layer. Note that the optimal interaction mechanism is very sensitive to the interfacial structure, which is in turn strongly dependent upon the initial conditions. Given the high cost of numerical simulations, we have not carried out a detailed study of this phenomenon. On the other hand, a gain of a few per cent in efficiency can be important for enhanced oil recovery processes, so that a detailed investigation of this phenomenon would appear to be a worthwhile pursuit.

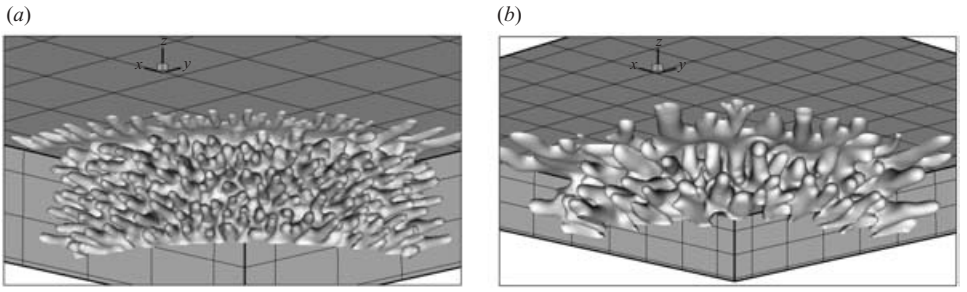

FIGURE 13. Concentration iso-surface for $Pe = 1,200$, $G = 0.5$, $R = 2.5$ and $A = 1/8$. A higher instability mode at this value of the Péclet number leads to the generation of small scales. Vigorous fingering starts very early in the simulation. Secondary instability in the form of tip splitting occurs throughout the displacement process. (*a*) $t = 0.04$, (*b*) $t = 0.12$.

5.2. *Influence of the Péclet number and the viscosity ratio*

The Péclet number has a strong effect on the most dangerous and the cutoff wavenumber, as well as on the instability growth rate, as shown by the linear stability analyses of Tan & Homsy (1987) and Riaz & Meiburg (2003). We expect that effect to carry over to the nonlinear regime, leading to more small-scale structure and intense fingering activity at high *Pe*. Furthermore, *Pe* is expected to play a prominent role in determining the balance between viscous and gravitational effects such as those observed in the previous section.

At a Péclet number of 1200, vigorous small-scale fingering occurs at the early time of $t = 0.04$, cf. figure 13(*a*). The effect of gravity override is confined to a very narrow gravity layer, and the fingering activity along the rest of the interface is nearly equally energetic. Already at this early time, secondary instabilities in the form of tip splitting and side branching events are evident at many locations. Together, merging and shielding events act to reduce the number of fingers significantly, as seen in figure 13(*b*). A very high flow rate established through the gravity layer gives rise to tip splitting events throughout the displacement process. This effect intensifies as the fingers near the diagonal race ahead and achieve breakthrough at $t = 0.174$. The breakthrough efficiency is reduced by about 17% as *Pe* is increased from 400 to 1200.

Regarding the effects of the viscosity ratio on the nonlinear displacement process, we again obtain some guidance from the linear stability analyses by Tan & Homsy (1987) and Riaz & Meiburg (2003). The growth rate as well as the most dangerous and the cutoff wavenumbers increase for larger viscosity ratios, for both vertical and horizontal perturbations. Consequently, we expect larger R values to lead to a more vigorous viscous instability, and to a change in the balance of viscous and gravitational effects.

We compare the two values of $R = 2.5$ and $R = 3.5$ at $t = 0.08$ in figure 14, for $Pe = 400$, $G = 0.5$ and $A = 1/8$. Both R values lead to the formation of a dominant gravity layer. The larger R value displays more intense fingering in both the gravity layer and the underride region. The displacement efficiency is reduced by 43% as R is increased from 2.5 to 3.5.

The relative magnitude of the vertical and horizontal viscous vorticity components as a function of *Pe* is shown in figure 15(*a*). It indicates that horizontal waves are amplified as *Pe* is increased from 400 to 800, whereas a further increase to $Pe = 1200$ does not enhance the vertical vorticity substantially. This behaviour is similar to our earlier observations for neutrally buoyant displacements, cf. figure 8. It is interesting

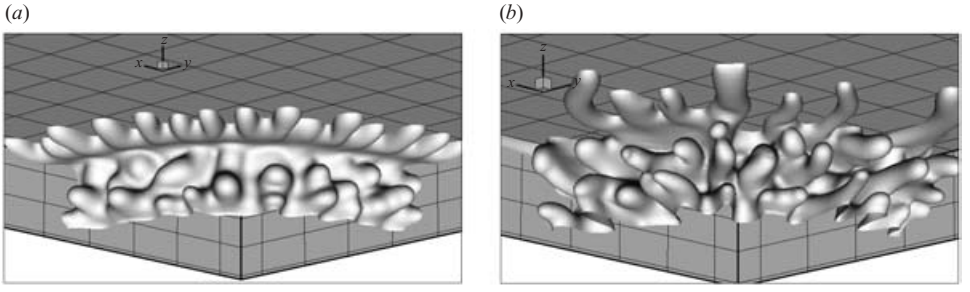

FIGURE 14. Concentration iso-surface for $Pe = 400$, $G = 0.5$, $A = 1/8$, $t = 0.08$, and (*a*) $R = 2.5$, (*b*) $R = 3.5$. Higher instability wavenumbers dominate at the higher value of R.

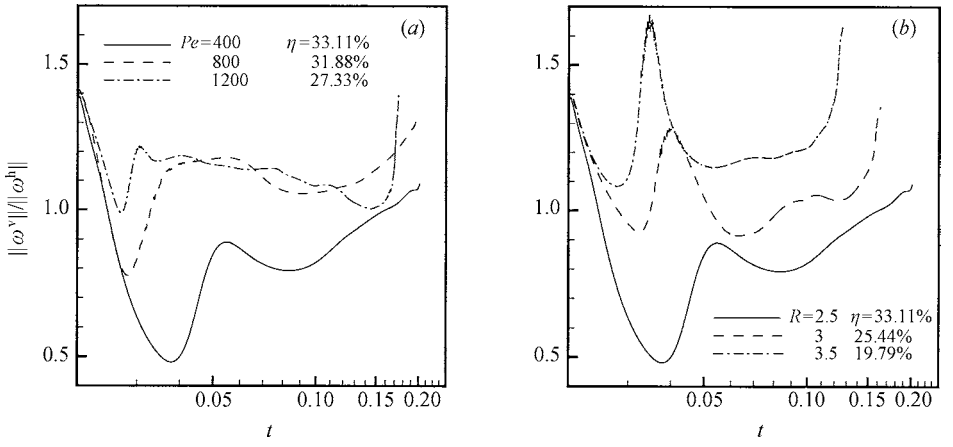

FIGURE 15. Ratio of the vertical to the horizontal viscous vorticity norm as a function of (*a*) Pe and (*b*) R, for $G = 0.5$, $A = 1/8$. Horizontal disturbances are monotonically amplified as R is increased. For $Pe = 1, 200$, $\|\omega^{\mathrm{v}}\|/\|\omega^{\mathrm{h}}\|$ does not increase further due to the nonlinear interactions among horizontal modes, which reduce the strength of the vertical viscous vorticity.

to note that, even though the ratio $\|\omega^{\mathrm{v}}\|/\|\omega^{\mathrm{h}}\|$ is quite similar for $Pe = 800$ and 1200, there is a significant difference in efficiency.

As a function of R, $\|\omega^{\mathrm{v}}\|/\|\omega^{\mathrm{h}}\|$ shows a monotonic increase (figure 15*b*). This indicates that high viscosity ratios do not lead to finger interactions that reduce the magnitude of the vertical viscous vorticity. Hence a very steep decline of the displacement efficiency is observed as R is increased from 2.5 to 3.5.

5.3. *Influence of the aspect ratio*

Displacement processes with gravity segregation are influenced by the domain aspect ratio. It was shown by Tchelepi (1994) and Ruith & Meiburg (2000) that for rectilinear flows gravity segregation becomes more important for smaller aspect ratios, as long and thin domains provide more time for the gravity override mechanism to operate. This holds true for the quarter five-spot domain as well. In order to demonstrate this, we plot $\|\omega^{\mathrm{v}}\|/\|\omega^{\mathrm{h}}\|$ for various aspect ratios in figure 16. As expected, smaller values of A exhibit a higher level of horizontal vorticity, which reflects a strengthening of the gravity override mechanism. Note that η diminishes with increasing A, in contrast to rectilinear displacements, where it was seen to be independent of A. For small A, the early dominance of the horizontal viscous vorticity reflects the existence of a

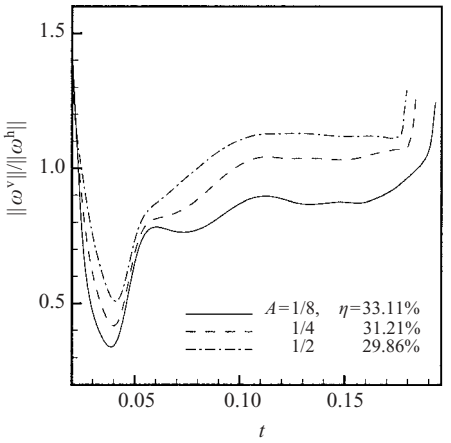

FIGURE 16. Influence of the aspect ratio. $Pe = 400$, $R = 2.5$, $G = 0.5$ and various values of A. Increase in A diminishes the influence of the gravity override mechanism which is observed as an increase in $\|\omega^v\|/\|\omega^h\|$.

strong gravity layer. The later increase in the vertical viscous vorticity is caused by the evolution of strong fingers in the gravity layer, which speed up its advance towards the production well.

6. Integral measures of the displacement processes

6.1. *Mixing length*

For miscible displacements, the mixing length l_{mix} represents an important one-dimensional diagnostic measure for capturing the overall dynamics of the displacement process. Therefore, there is a wide ranging practical interest in quantifying the growth rate of the mixing length. We employ the definition of Chen & Meiburg (1998*a*) for the mixing length in quarter five-spot displacements.

For rectilinear and quarter five-spot flows, l_{mix} grows proportionally to $t^{1/2}$ during the initial linear phase as a result of the diffusive spreading of the concentration front. During the later nonlinear phase, a larger exponent reflects the dominant convective effects. While the exact value of the exponent is sensitive to the parameter regime, the asymptotic rate of growth is found to be ≈ 1.5 for rectilinear flows, cf. Tan & Homsy (1988), and ≈ 1 for two-dimensional quarter five-spot flows, as shown by Chen & Meiburg (1998*a*).

The evolution of l_{mix} goes through three separate phases with distinct growth exponents, figure 17. During the first, linear phase, the perturbation amplitude is still small, and the mixing length grows primarily as a result of diffusion. Note that the evolution of l_{mix} is independent of the gravity parameter, a fact also observed for two-dimensional rectilinear displacements (Ruith & Meiburg 2000).

The growth of viscous fingers in the axisymmetric base flow near the source characterizes the second, strongly parameter dependent phase of rapid growth. During this second phase, the rate of growth of l_{mix} increases with both R and Pe, according to $\approx R^{1.1}$ and $\approx Pe^{0.6}$, respectively. These power law dependencies of l_{mix} on R and Pe are similar to those found for the instability growth rates, cf. Riaz & Meiburg (2003), namely, R^1 and $\approx Pe^{0.5}$.

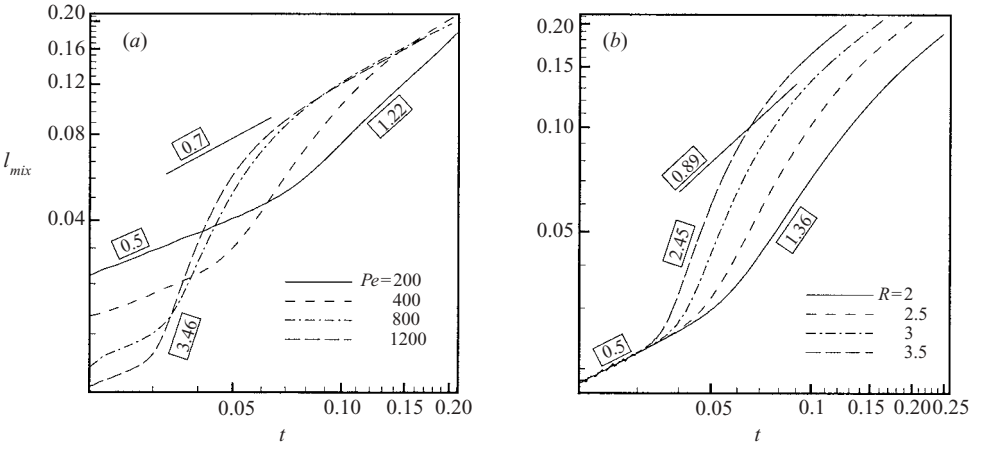

FIGURE 17. Mixing length *vs.* time, (*a*) as a function of Pe at $R = 2.5$, $G = 0.5$ and $A = 1/8$, and (*b*) as a function of R at $Pe = 400$, $G = 0.5$ and $A = 1/8$. Boxed numbers represent growth exponents. A three-phase behaviour is observed for the evolution of l_{mix}, i.e. an initial diffusive growth, a faster than linear growth at intermediate times, and a late-time asymptotic growth. The last two regimes are parameter dependent for small values of Pe, while a constant value of 0.7 is approached for large Pe. The second phase is more sensitive to variation in R, while the R-independent final phase is observed to have a growth rate of 0.89.

The growth rate of l_{mix} drops in the third phase as a result of nonlinear finger interactions. The late time value of the mixing length growth exponent varies only with the Péclet number, and for high Péclet numbers a parameter independent value of ≈ 0.7 is approached. The variation of the growth rate of l_{mix} as a function of Pe, and its independence of R, highlight a fundamental difference in the influence of Pe and R on the displacement process. Large values of Pe encourage a higher level of nonlinear finger interactions such as merging and shielding, which rapidly reduce the mixing length growth rate. On the other hand, large values of R do not give rise to the same level of finger interaction, such that flow paths, once they are established, are relatively free from interactions with neighbouring fingers, as shown in figure 14.

6.2. *Interfacial area*

The overall growth of the interfacial area by stretching and folding represents an important quantity, especially for displacements in which chemical reactions can occur along the concentration front (De Wit & Homsy 1999, Demuth & Meiburg 2003). We employ the following definition of the overall interfacial area

$$\boldsymbol{\Lambda}(t) = \int_0^A \int_0^1 \int_0^1 \left(c_x^2 + c_y^2 + c_z^2\right)^{1/2} \mathrm{d}x\, \mathrm{d}y\, \mathrm{d}z. \tag{6.1}$$

Figure 18 indicates that the interfacial area evolves similarly to the mixing length, i.e. in three phases. It is also independent of G. Initially, the interface area grows as $t^{1/2}$ for all cases. Thereafter, a nonlinear phase follows which is characterized by a growth exponent that increases with Pe and R. This reflects the more vigorous growth of the viscous fingers for larger Péclet numbers and viscosity ratios. In contrast to l_{mix}, the magnitude of the interfacial area does not tend to become independent of Pe. An approximate asymptotic growth exponent of 0.6 is observed as a function of both Pe and R. Since a stable interface would grow as $t^{1/2}$, the late time growth exponent of 0.6 indicates a fairly small effect of the fingers on the overall interfacial area growth.

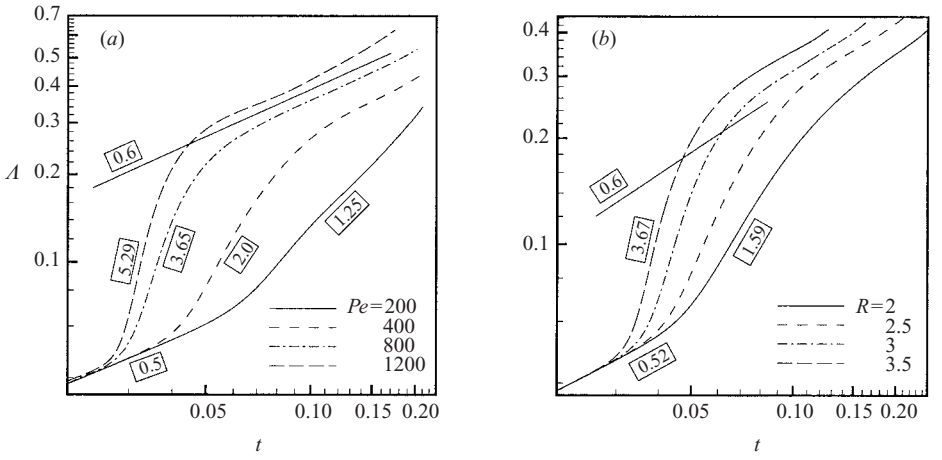

FIGURE 18. Interfacial area Λ vs. time, (a) as a function of Pe at $R = 2.5$, $G = 0.5$ and $A = 1/8$, and (b) as a function of R at $Pe = 400$, $G = 0.5$ and $A = 1/8$. Λ strongly depends on both Pe and R. An asymptotic rate of growth of ≈ 0.6 is observed for large times and all parameter combinations.

6.3. *Gravity-layer thickness*

For displacements involving gravity override, an analysis of the gravity-layer thickness is of interest. Closed form expressions for the thickness of the finger as a function of the gravity parameter have been reported by Brener, Levine & Tu (1991), Brener, Rabaud & Thome (1993) and by Zhan & Yortsos (2002) for immiscible flows in a Hele-Shaw cell. Corresponding analytical expressions are not available for the miscible displacement case. Based on numerical simulations of rectilinear displacements, Ruith & Meiburg (2000) provide a scaling law for the gravity-layer thickness d:

$$d \propto G^{1/2} Pe^{-1/2}.$$

For the quarter five-spot case, we obtain the following scaling law:

$$d \propto G^{0.2} Pe^{-0.6}.$$

A uniform scaling as a function of R is not observed. In contrast to immiscible displacements, where d decreases as the gravity parameter is increased (Zhan & Yortsos 2002), miscible displacements show an increase in d with G.

7. Conclusions

The present investigation employs high-accuracy numerical simulations in order to analyse three-dimensional miscible displacements with gravity override in the quarter five-spot geometry. Even for neutrally buoyant displacements, three-dimensional effects are seen to change the character of the flow in a way that cannot be anticipated from two-dimensional simulations alone. This is in contrast to the case of rectilinear miscible flows, for which Zimmerman & Homsy (1992*a*) and Tchelepi & Orr (1994) found the inclusion of the third dimension to have generally small effects. Part of the difference between two- and three-dimensional quarter five-spot flows can be attributed to the enhanced interaction of disturbances in three dimensions, resulting from the time dependence of the most amplified axial mode (Riaz & Meiburg 2003).

By forcing a large-scale redistribution of concentration gradients, the temporal change of the axial wavenumber introduces an additional source of instability in the system.

Density differences have a significant influence on the displacement, primarily through the production of a narrow gravity layer which bypasses much of the resident fluid to arrive at the production side ahead of the underride region, thereby reducing the displacement efficiency. However, for certain parameter combinations buoyancy forces of the right magnitude can pinch off the gravity layer and hinder its movement towards the production well.

The interaction of viscous and gravitational effects is analysed on the basis of their respective contributions to the temporal evolution of the vorticity field. The gravitational effect is associated with an increase in the horizontal vorticity component, while the viscous effect is related to both horizontal and vertical vorticity components. As expected, the gravitational effect primarily operates on vertical disturbances. Somewhat surprisingly, however, an increase in either Pe or R affects vertical and horizontal disturbances differently. While the horizontal modes are increasingly amplified as the viscosity ratio is increased, a nonlinear saturation is observed for them as a function of the Péclet number.

With respect to integral measures characterizing the displacement process, the asymptotic rate of growth of the mixing length varies only with Pe. It is seen to become independent of the Péclet number for large Pe, when the growth exponent approaches the value of ≈ 0.7. This value is different from an asymptotic value of ≈ 1 obtained for two-dimensional quarter five-spot displacements. The total interfacial area is seen to grow with an asymptotic exponent of ≈ 0.6 for all parameter combinations, except for very low Pe values.

The present analysis of homogeneous displacements represents an important first step on the way towards understanding fully heterogeneous displacements. First of all, the basic mechanism of viscous instability persists in the presence of heterogeneity and, the response of the viscous vorticity field to excitations in the form of heterogeneity is closely related to the fundamental viscous instability mechanism (De Wit & Homsy 1997*a*). Secondly, for small values of the heterogeneity variance and the correlation length, the displacement is essentially homogeneous. The next step will be to address the issue of how the displacement mechanisms in homogeneous displacements are modified by the existence of permeability heterogeneities. Earlier two-dimensional investigations of heterogeneous rectilinear (Tan & Homsy 1992; De Wit & Homsy (1997*a*, *b*; Camhi, Ruith & Meiburg 2000) and quarter five-spot flows (Chen & Meiburg 1998*b*) indicate the existence of different parameter regimes characterized by fundamentally different interactions of the viscosity, density and permeability related vorticity contributions. An investigation of how this interplay is affected by the presence of the third dimension is currently underway.

The authors thank Dr Hamdi Tchelepi for several helpful discussions. Support for this research by the Petroleum Research Fund, the Department of Energy, Chevron Petroleum Technology Company, as well as through an NSF equipment grant and the San Diego Supercomputer Center is gratefully acknowledged.

REFERENCES

Ben, Y., Demekhin, E. A. & Chang, H.-C. 2002 A spectral theory for small-amplitude miscible fingering. *Phys. Fluids* **14**, 999.

Bradvedt, F., Bradvedt, K., Buchholz, C. F., Holden, H., Holden, K. & Risebro, N. H. 1992 A new front-tracking method for reservoir simulation. *SPE Res. Engng*, p. 107.

Brady, J. F. & Koch, D. L. 1988 *In Disorder and Mixing*. NATO ASI series E. Academic.

Brand, C. W., Heinemann, J. E. & Aziz, K. 1991 The grid orientation effects in reservoir simulation. *SPE Paper* **21228**, 275.

Brener, E., Levine, H. & Tu, Y. 1991 Nonsymmetric Saffman–Taylor fingers. *Phy. Fluids* **3**, 529.

Brener, E., Rabaud, M. & Thome, H. 1993 Effect of gravity on stable Saffman–Taylor fingers. *Phys. Rev.* E **48**, 1066.

Camhi, E., Ruith, M. & Meiburg, E. 2000 Miscible rectilinear displacements with gravity override. Part 2. Heterogeneous porous media. *J. Fluid Mech.* **420**, 259.

Canuto, C., Hussaini, M. Y., Quarteroni, A. & Zang, T. A. 1986 *Spectral Methods in Fluid Dynamics*. Springer Series in Computational Dynamics. Springer.

Caudle, B. H. & Witte, M. D. 1959 Production potential changes during sweep out in a five-spot system. *Trans. AIME* **216**, 446.

Chen, C.-Y. & Meiburg, E. 1998*a* Miscible porous media displacements in the quarter five-spot configuration. Part 1. The homogeneous case. *J. Fluid Mech.* **371**, 233.

Chen, C.-Y. & Meiburg, E. 1998*b* Miscible porous media displacements in the quarter five-spot configuration. Part 2. Effect of heterogeneities. *J. Fluid Mech.* **371**, 269.

Chen, C.-Y. & Meiburg, E. 2000 High-accuracy implicit finite-difference simulations of homogeneous and heterogeneous miscible porous medium flows. *SPE J.* **5**, 129.

Chouke, R. L., Meurs, P. V. & Poel, C. V. D. 1959 The instability of slow, immiscible, viscous liquid–liquid displacements in permeable media. *Trans. AIME* **216**, 188.

Christie, M. A. & Bond, D. J. 1987 Detailed simulation of unstable processes in miscible flooding. *SPE Res. Engng*, p. 514.

De Wit, A. & Homsy, G. M. 1997*a* Viscous fingering in periodically heterogeneous porous media. I. Formulation and linear stability. *J. Chem. Phys.* **107**, 9609.

De Wit, A. & Homsy, G. M. 1997*b* Viscous fingering in periodically heterogeneous porous media. II. Numerical simulations. *J. Chem. Phys.* **107**, 9619.

De Wit, A. & Homsy, G. M. 1999 Nonlinear interactions of chemical reactions and viscous fingering in porous media. *Phy. Fluids* **11**, 949.

Demuth, R. & Meiburg, E. 2003 Chemical fronts in Hele-Shaw cells: linear stability analysis based on the three-dimensional Stokes equations. *Phys. Fluids* **15**, 597.

Fayers, F. J., Blunt, M. J. & Christie, M. A. 1992 Comparisons of empirical viscous fingering models and their calibration for heterogeneous problems. *SPE Res. Engng*, p. 195.

Gottlieb, D. & Orszag 1977 *Numerical Analysis of Spectral Methods: Theory and Applications*. Society for Industrial and Applied Mathematics.

Habermann, B. 1960 The efficiency of miscible displacement as function of mobility ratio. *Trans. AIME* **219**, 264.

Hill, S. 1952 Channeling in packed columns. *Chem. Engng Sci.* **1**, 247.

Homsy, G. M. 1987 Viscous fingering in porous media. *Annu. Rev. Fluid Mech.* **19**, 271.

Horne, R. N. & Rodriguez, F. 1983 Dispersion in tracer flow in fractured geothermal systems. *Geophys. Res. Lett.* **10**, 289.

Lacey, J. W., Faris, J. E. & Brinkman, F. H. 1961 Effect of bank size on oil recovery in the high pressure gas-driven LPG-bank process. *T. Soc. Petrol. Engr. AIME* **222**, 806.

Lele, S. K. 1992 Compact finite differences with spectral-like resolution. *J. Comput. Phys.* **103**, 16.

Meiburg, E. & Homsy, G. M. 1988*a* Nonlinear unstable viscous fingers in Hele-Shaw flows. II. Numerical simulation. *Phys. Fluids* **31**, 429.

Meiburg, E. & Homsy, G. M. 1988*b* Vortex methods for porous media flows. In *Numerical Simulation in Oil Recovery*. IMA volumes in Mathematics and its Applications 11. Springer.

Morel-Seytoux, H. J. 1965 Analytical–numerical method in water flooding predictions. *SPE J.* Sept. 247.

Pankiewitz, C. & Meiburg, E. 1999 Miscible porous media displacements in the quarter five-spot configuration. Part 3. Non-monotonic viscosity profiles. *J. Fluid Mech.* **388**, 171–195.

Perkins, T. K., Johnston, O. C. & Hoffman, R. N. 1965 Mechanics of viscous fingering in miscible systems. *SPE J.* **5**, 301.

Petitjeans, P., Chen, C.-Y., Meiburg, E. & Maxworthy, T. 1999 Miscible quarter five-spot displacements in a Hele-Shaw cell and the role of flow-induced dispersion. *Phys. Fluids* **11**, 1705.

Riaz, A. 2003 Three-dimensional miscible, porous media displacements in the quarter five-spot geometry. PhD thesis, Department of Mechanical and Environmental Engineering, University of California, Santa Barbara.

Riaz, A. & Meiburg, E. 2002 Three-dimensional vorticity dynamics of miscible porous media flows. *J. Turbul.* **3**, 61.

Riaz, A. & Meiburg, E. 2003 Radial source flows in porous media: linear stability analysis of axial and helical perturbations in miscible displacements. *Phys. Fluids* **15**, 938.

Rogerson, A. & Meiburg, E. 1993*a* Numerical simulation of miscible displacement processes in porous media flows under gravity. *Phys. Fluids* **5**, 2644.

Rogerson, A. & Meiburg, E. 1993*b* Shear stabilization of miscible displacements in porous media. *Phy. Fluids* **5**, 1344.

Ruith, M. & Meiburg, E. 2000 Miscible rectilinear displacements with gravity override. Part 1. Homogeneous porous medium. *J. Fluid Mech.* **420**, 225.

Saffman, P. G. & Taylor, G. I. 1958 The penetration of a fluid into a porous medium or Hele-Shaw cell containing a more viscous liquid. *Proc. R. Soc. Lond.* A **245**, 312.

Sherwood, J. D. 1987 Unstable fronts in a porous medium. *J. Comput. Phys.* **68**, 485.

Simmons, J., Landrum, B. L., Pinson, J. M. & Crawford, P. B. 1959 Swept areas after breakthrough in vertically fractured five-spot patterns. *Trans. AIME* **216**, 73.

Slobod, R. L. & Thomas, R. A. 1963 Effect of tranverse diffusion on fingering in miscible-phase displacement. *SPE J.* **3**, 9.

Tan, C. T. & Homsy, G. M. 1987 Stability of miscible displacements in porous media: radial source flow. *Phys. Fluids* **30**, 1239.

Tan, C. T. & Homsy, G. M. 1988 Simulation of nonlinear viscous fingering in miscible displacement. *Phys. Fluids* **31**, 1330.

Tan, C. T. & Homsy, G. M. 1992 Viscous fingering with permeability heterogeneity. *Phys. Fluids* **4**, 1099.

Taylor, G. I. 1953 Dispersion of soluble matter in solvent flowing slowly through a tube. *Proc. R. Soc. Lond.* A **219**, 186.

Tchelepi, H. A. 1994 Viscous fingering, gravity segregation and permeability heterogeneity in two dimensional and three dimensional flows. PhD thesis, Department of Petroleum Engineering, School of Earth Sciences, Stanford University.

Tchelepi, H. A. & Orr, F. M. J. 1993 Dispersion, permeability heterogeneity and viscous fingering: acoustic experimental observations and particle tracking simulations. *Phys. Fluids* **5**, 1558.

Tchelepi, H. A. & Orr, F. M. J. 1994 Interaction of viscous fingering, permeability inhomogeneity and gravity segregation in three dimensions. *SPE Res. Engng*, p. 266.

Tryggvason, G. & Aref, H. 1985 Finger interaction mechanisms in stratified Hele-Shaw flow. *J. Fluid Mech.* **154**, 287.

Wooding, R. A. 1969 Growth of fingers at an unstable diffusing interface in a porous medium or Hele-Shaw cell. *J. Fluid Mech.* **39**, 477.

Wray, A. A. 1991 Minimal storage time-advancement schemes for spectral methods. Preprint.

Yortsos, Y. C. & Zeybek, M. 1988 Dispersion driven instability in miscible displacement in porous media. *Phys. Fluids* **31**, 3511.

Zhan, L. & Yortsos, Y. C. 2002 The shape of a gravity finger in a rectangular channel in homogeneous porous media. *Transport Porous Media* **49**, 77.

Zhang, H. R., Sorbie, K. S. & Tsibuklis, N. B. 1997 Viscous fingering in five-spot experimental porous media: new experimental results and numerical simulations. *Chem. Engng Sci.* **52**, 37.

Zimmerman, W. B. & Homsy, G. M. 1992*a* Three-dimensional viscous fingering: A numerical study. *Phys. Fluids* **4**, 1901.

Zimmerman, W. B. & Homsy, G. M. 1992*b* Viscous fingering in miscible displacements: Unification of effects of viscosity contrast, anisotropic dispersion and velocity dependence of dispersion on nonlinear finger propagation. *Phys. Fluids* **4**, 2348.